6

SPLEEM

E. Bauer

Spin-polarized low energy electron microscopy is one of several methods for the study of the magnetic microstructure of surfaces and thin films on surfaces. It is a non-scanning, full-field imaging method that allows much faster image aquisition than scanning methods, provided that the electrons are elastically backscattered along or close to the optical axis of the instrument. This is the case in single crystals and epitaxial films or films with strong fiber texture. After a brief introduction (6.1), this chapter first discusses the physics of the electron beam–specimen interaction that is the basis of SPLEEM (6.2). This is followed by a brief description of the experimental aspects of the method (6.3). The remaining part is devoted to the applications of SPLEEM mainly in the study of thin film systems (6.4). The final section (6.5) briefly summarizes the possibilities and limitations of the method.

6.1 Introduction

SPLEEM (spin-polarized low energy electron microscopy) is an imaging method that is based on the spin dependence of the elastic backscattering of slow electrons from ferromagnetic surfaces. It is related to SPLEED (spin-polarized low energy electron diffraction) in the same manner as LEEM is to LEED. SPLEEM differs from LEEM in that the incident beam is partially spin-polarized, always normal to the surface, and only the specularly reflected beam and its close environment is used for imaging, while in LEEM sometimes tilted illumination or other diffracted beams are used. The normal incidence and reflection ensures, at least in the absence of multiple scattering, that spin-orbit interaction is not contributing to the signal, so that the magnetic contribution to the signal results from only the exchange scattering.

The first demonstration of the ability of spin-polarized slow electrons to provide information on the state of magnetization of a magnetic material was performed by Celotta et al. [1]. They used the specular reflection of 125 eV electrons incident at 12° from the normal of an in-plane magnetized thin Ni(110) crystal to measure the hysteresis curve and the temperature dependence of the magnetic contribution to the reflected intensity. When LEEM had demonstrated its possibilities in the late 1980s, one of the pioneers in the field, D. Pierce, suggested adding a spin-polarized gun to the LEEM system and looking at magnetic properties with high lateral resolution. It took, however, some strong stimulation-provided by H. Poppa – and financial support from a research laboratory strong in thin film magnetics, IBM Almaden Research Center, to follow up this suggestion more than 20 years after the first SPLEED experiments. The first results were reported in 1991 [2], and since then, the method has developed very slowly, in part due to the complexity of the systems, in part due to relocation and personnel changes.

SPLEEM has many of the possibilities and limitations that LEEM and SPLEED have. With LEEM, for example, it shares the resolution limitations, with SPLEED the fact that quantitative analysis is complicated by spin-dependent multiple scattering and attenuation. The main strengths are its high surface sensitivity and rapid image acquisition. The possibilities and limitations are in part determined by the beam-specimen interaction, in part by the instrument, i.e., the electron source, the electron optics, and the image detection.

6.2 Physical Basis of Beam-Specimen Interactions

As mentioned in the introduction, it is the exchange interaction between the spin-polarized beam electrons and the spin-polarized electrons in the ferromagnetic material – a consequence of the Pauli principle – that makes SPLEEM magnetization sensitive. Slater [3] has shown that this interaction can be represented by an exchange potential V_x that has to be added to the Coulomb potential V_c. V_c describes the interaction of an electron with the nuclei and all electrons, including itself. The original form of V_x was $-3[(3/8\pi)\rho]^{1/3}$, where ρ is the charge density. Hammerling et al. [4] and Kivel [5] were the first to use a potential of this form to calculate scattering cross sections of free atoms for very slow electrons ($E < 2\,\text{eV}$) successfully. Calculations over a wider energy range [6], however, gave acceptable agreement with experiment only when different $V_{x\ell}$ were used for different orbitals. The agreement could be further improved [7] when the energy dependence

$$F(\eta) = 1/2 + [(1-\eta^2)/4\eta]\ln[(1+\eta)/(1-\eta)] \tag{6.1}$$

of the exchange potential of the free electron gas [8] was taken into account, so that

$$V_x(\eta) = -4[(3/8\pi)\rho]^{1/3}F(\eta)\,, \tag{6.2}$$

where $\eta = k/k_F$, k being the wave number of an electron with kinetic energy $\hbar^2k^2/2m$ and $k_F = (3\pi^2\rho)^{1/3}$ the Fermi wave number. Experience with the application of this potential to atomic calculations has shown that the original expression overestimates the influence of the "exchange hole", which can be taken into account by a factor of about 2/3 [9]. The scattering calculations mentioned above were made without regard to spin, that is for unpolarized beam and target. When the spin polarization of the electron or of the target is of interest, a more sophisticated treatment is needed, as described in Chap. 3 and 4 of [10]. However, for atoms for which the Thomas-Fermi-Dirac model of the electronic structure is a reasonable approximation, the exchange interaction may be approximated again with an energy-dependent Slater-type potential for spin up and spin down charge densities separately. The good agreement that Slater et al. [9] obtained with various forms of V_x for the various ground state quantities of the closed shell ion Cu^+ suggests that $V_x^{\uparrow}(\eta)$ and $V_x^{\downarrow}(\eta)$ should also be good approximations of the exchange interactions with spin up and spin down electrons, respectively, in electron scattering.

In the elastic scattering of slow spin-polarized electrons from crystals, that is, in SPLEED, not only is the energy- and spin-dependent exchange potential of importance, but also proper inclusion of multiple scattering. This is due to the fact that the wave field incident on a given atom is not only the plane wave incident from the outside, but consists also of the waves scattered by the surrounding atoms. The multiple scattering ("dynamical") theory required in this case has reached a high level of sophistication in LEED and has also been developed for SPLEED mainly by Feder and has been well reviewed by him [10–12]. In this theory, the diffracted intensity is calculated for positive and negative V_x contribution corresponding to the scattering of electrons with spin parallel and anti-parallel to the spins in the magnetic material. The magnetic signal, the so-called scattering asymmetry, is obtained from the normalized intensity difference

$$A = (I_+ - I_-)/(I_+ + I_-)\,. \tag{6.3}$$

A discussion of the SPLEED theory is beyond the scope of this review, particularly since very little theoretical work has been done for the conditions used in SPLEEM (180° scattering, very low energies). In the energy range of SPLEEM ($< 10\,\mathrm{eV}$) fewer partial waves are needed and the exchange potential is significantly stronger than at the usual SPLEED energies. For a typical SPLEEM energy (2 eV) V_x is about four times larger than at a typical SPLEED energy (50 eV) for Fe, Co, and Ni. In the scattering from the solid state potentials of these atoms – whose energy zero is the muffin tin zero – the phase of the $l = 2$ partial wave passes through $\pi/2$ near the vacuum level. This causes strong backward scattering that is different for spin-up and spin-down electrons because of the different V_x contributions $(+/-V_x)$. As a consequence, A is large at these energies. Of course, the spin-independent part of the backward scattering is also large, which facilitates focusing and astigmatism correction. As a consequence of multiple scattering, the connection between scattering asymmetry and magnetization is not straightforward. It is generally accepted that the magnetization is layer-dependent. First-principle calculations give enhancements ranging from a few percent to about 50% for the topmost layer that decrease rapidly to the bulk value within a few atomic layers. SPLEED calculations for various layer profiles show [13]:

i) the top layer magnetization M_s determines A if all other layers have bulk magnetization M_b, but A is not proportional to M_s or some average magnetization;
ii) if all layers have the same magnetization M, then A is proportional to $M = M_s = M_b$;

iii) if the layer dependence of the magnetization M_n is homogeneous, then A is proportional to M_s.

These results are for a rigid lattice ($T = 0$). Thermal vibrations reduce the spatial coherence in multiple scattering and relax these limitations somewhat. The temperature dependence of the magnetic correlation length ξ plays a more important role. If ξ is large compared with the thickness contributing to the scattering, then the M_n scale is like M_s. ξ becomes large in the temperature range close to the Curie temperature T_C, in which the asymptotic power laws of the critical behavior are valid.

These theoretical considerations for SPLEED, wich are at least to some extent also valid for SPLEEM, suggest that SPLEED and SPLEEM give information on the surface magnetization and its critical behavior if used with proper caution. To which extent this is the case can only be decided by a comparison between theory and experiment. A test case for the ability of SPLEED to determine the magnetization profile M_n ($n = 1 = s, 2, 3, 4$) is the Fe(110) surface. Theory [14] predicts enhancement factors M_n/M_b of 1.194, 1.068, 1.027, and 1.014 in the first four layers over the bulk magnetization. The experimental SPLEED data for thin Fe(110) films on W(110) of Waller and Gradmann [15] were analyzed by two groups. Tamura et al. [16] analyzed the experimental data for 62 eV and concluded $M_1/M_b = 1.35$ and $M_2/M_b = 0.85$, confirming an earlier, less detailed analysis [17]. Ormeci et al. [18,19] simulated the theoretical M_n/M_b data [14] in their model calculations and obtained equally good agreement with the experimental data for 62 eV, but found little sensitivity to changes of M_1/M_b at other energies. On the other hand, a large surface enhancement is also deduced from magnetometric measurements [20]. Thus, it appears difficult to extract magnetization profile information from SPLEED measurements. A similar conclusion was drawn by Plihal et al. [21] from a comparison of SPLEED calculations with experimental results for the Fe double layer on W(100). On the Ni(100) surface, an enhancement in the range from 0 to 10% was found [22], in agreement with theoretical values of 5.8–6.8%. On the Ni(111) surface $M_s/M_b = 0.9$–1.3 was deduced from a theory-experiment comparison [23] in agreement with the theoretical value 1.16.

These comparisons show that there is considerable uncertainty regarding the relation between A and M. Two observations are of interest in this connection. Kirschner [24] found in his study of the temperature dependence of A of a Fe(110) surface strong deviations from the expected behavior in the 10 eV range, while the $A(T)$, measured at 3.5 eV, fitted the bulk behavior quite well. Elmers and Hauschild [25] found characteristic deviations from the asymptotic power law $A(T) \propto (T_C - T)^\beta$ for Fe films on W(100) that were thicker than two monolayers. These observations suggest the use of either very slow electrons, that is to work in the SPLEEM energy range or to restrict the measurements to thicknesses below two monolayers if reliable information on M is to be derived from A, or to use A only as an indicator of the magnetic behavior. The latter philosophy was adopted in a study of Fe films on W(100) [26], the second has been followed with considerable success in Gradmann's group, and the results have been well reviewed by Elmers [27]. More work of this kind, all on Fe films on W(110) and W(100) can be found in references [28–30]. The first philosophy is the basis of recent SPLEEM studies of the magnetization of thin Fe films on Cu(100) [31] and of Co films on W(111) [32], which will be discussed below.

As pointed out earlier, at very low energies, the phase of the $l = 2$ partial wave passes through $\pi/2$, causing strong spin-dependent backscattering and, thus, a significant A. This simple picture is applicable in the case of amorphous or polycrystalline samples. In single crystals, the band structure also plays an important role, as illustrated in Fig. 6.1 for a Co(0001) surface. The band structure in the ΓA direction ([0001] direction) is exchange-split with an exchange splitting between 1.0 and 1.6 eV, depending upon the computational method. Below the two bands there is a 6–7 eV wide band gap in which the wave number k is imaginary. The material acts as a reactive medium with (theoretically) 100% reflectivity. When the electron energy is increased from zero to the onset of the spin-up band, the reflectivity for spin-up electrons suddenly decreases, while the spin-down electrons are still 100% reflected until the onset of the spin-down band is reached. Therefore, A is negative between the two band onsets. With further increasing energy, A is also nonzero, because of the slightly different density of states at a given energy. This picture has to be refined below by the inclusion of inelastic processes. Figure 6.1 also shows that the k-values of spin-up and spin-down electrons at a given energy differ. This has important consequences for thin film studies in which "quantum size effects" occur due to the interference effects in thin films well known from optics: Whenever the wave length $\lambda = 2t/n$ (n integer), the reflectivity has a maximum that occurs at a different thickness for spin-up and spin-down electrons because of $\lambda_\uparrow \neq \lambda_\downarrow$. A also oscillates with energy because the interference condition is fulfilled for different energies for spin-up and spin-down electrons. Fig. 6.2 illustrates this for a 6 monolayer thick Co film on W(110) [33]. The oscillations are clearly seen despite the fact that the film is a three-level system consisting of 5, 6 and 7 monolayer thick regions. At the first quantum size resonance the asymmetry is much larger than upon reflection from the surface of a thick crystal that can be utilized for very efficient polarization detection. The experimental data could be well fitted with SPLEED calculations [34].

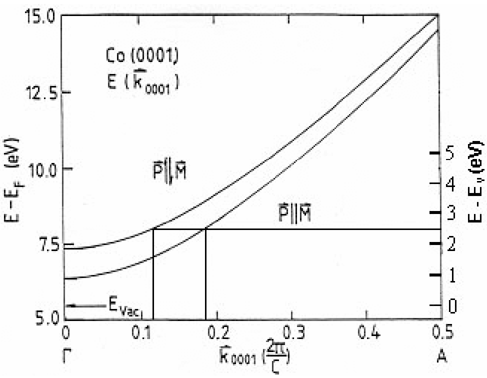

Fig. 6.1. Band structure of Co in the ΓA direction ([0001]) above the vacuum level

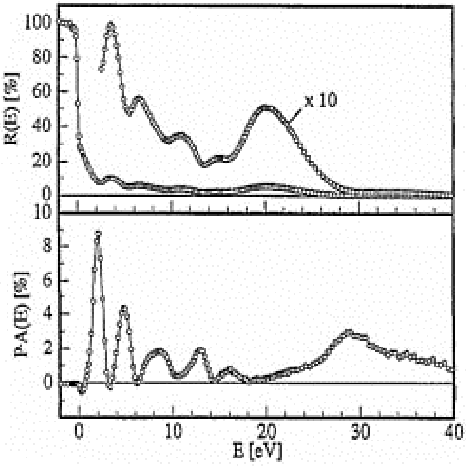

Fig. 6.2. Intensity (top) and asymmetry (bottom) of the specular beam from a six-mono-layer-thick epitaxial Co layer with (0001) orientation on a W(110) surface as a function of electron energy

The discussion up to now did not take into account inelastic scattering. Except for the elastic attenuation of the incident wave at energies in the band gaps, inelastic scattering is the main factor that determines the sampling depth of slow electrons. At the low energies generally used in SPLEEM, $3p \rightarrow 3d$ excitations, which have been considered important in the SPLEED energy range [22,23], and plasma excitations do not occur, only electron-hole pair creation, phonon, and magnon excitations occur. The last two processes involve small energy losses ("quasi-elastic scattering") and cannot be separated from elastic scattering in SPLEEM because of insufficient energy resolution. Phonon excitation attenuates the reflected beam irrespective of its polarization because of the large momentum change associated with them and the small transverse momentum acceptance of the SPLEEM instrument dictated by the large aberrations of the objective lens. Magnon excitation is possible only by spin-down electrons. It involves a spin flip and thus increases the number of spin-up electrons upon reflection, that is, it changes the polarization of the beam. The cross section for magnon excitation has long been considered to be orders of magnitudes smaller than that for the (spin-conserving) phonon and elastic scattering [35,36]. Recent detailed calculations for Fe and Ni by Hong and Mills [37] have confirmed this for electron energies above the vacuum level, but at the same time have shown that magnon excitation is an important damping mechanism in Fe for electrons close to the Fermi level. In the energy range of SPLEEM, magnon excitation may be neglected.

Electron-hole pair creation can occur with spin-flip (Stoner excitations) or without spin-flip (direct excitations). Both excitations attenuate the signal when the momentum change is larger than that accepted by the angle-limiting aperture, or when the energy change is so large that the electron is deflected outside the angle-limiting aperture by the dispersion of the beam separator. In practice, the second attenuation effect is unimportant because of the small energy change, the weak dispersion, and the aperture sizes used. In addition to the attenuation, Stoner excitations with sufficiently small momentum and energy transfer (so that the reflected electron is accepted by the angle-limiting aperture) change the polarization of the reflected beam. In these excitations, a spin-down (spin-up) electron drops into an empty minority (majority) spin state and excites via an exchange process a majority (minority) spin electron to the final state with a lower energy than that of the incident electron. Because the density of unoccupied minority spin states is much larger than that of the majority spin states, this process effectively increases (decreases) the number of spin-up (spin-down) electrons in the reflected beam. This is best seen in the case of Ni, in which the majority spin band is completely filled [38].

As a consequence, the total inelastic scattering cross section σ is spin-dependent and is given for spin-up ($\sigma_\uparrow$) and spin-down ($\sigma_\downarrow$) electrons to a first approximation by [39]

$$\sigma_{\uparrow\downarrow} = \sigma_o + \sigma_d(5 - n_{\uparrow\downarrow})\,. \tag{6.4}$$

Here σ_d is the cross section for scattering into an unoccupied d-orbital, σ_o the cross section for scattering into all other non-d-orbital, and $n_\uparrow$, $n_\downarrow$ are the numbers of occupied majority and minority spin states, respectively. These cross sections may differ by a factor as large as three [40]. Recent model calculations for Fe, Co, and Ni [41] and explicit calculations for Fe and Ni [37] confirm the general trend with the number $5 - n_{\uparrow\downarrow}$ of d-holes, but show that the relationship is not linear. Figure 6.3 [37] shows the inelastic mean free paths $l_\uparrow$ and $l_\downarrow$ for spin-up and spin-down electrons in Fe and Ni derived from the imaginary part of the self-energy of an electron with energy E above the Fermi level. The work functions of Fe(110) and Ni(111) surfaces are approximately 5.1 and 5.55 eV. Although the largest differences between $l_\uparrow$ and $l_\downarrow$ occur below the vacuum level, they are still significant in the SPLEEM energy range: In Fe $l_\uparrow/l_\downarrow \approx 3.2$, in Ni $l_\uparrow/l_\downarrow \approx 1.8$ at 1 eV above vacuum level. 5 eV above the Fermi level, this ratio is still about 2.0 for Fe, while in Ni it has already decreased to about 1, that is, the IMFP is already spin-independent [37]. From experiment, however, a ratio of about 3 has been deduced for Ni at a still higher energy (12 eV above the vacuum level) [38]. Thus, there is still some uncertainty in the magnitude of the difference of the two IMFPs, but there is no doubt that spin-down electrons are damped more than spin-up electrons.

A comparison of the IMFPs with the elastic attenuation lengths in band gaps suggests that the importance of band gaps for the magnetic contrast, as determined by the asymmetry A, has been overestimated in the past. As an example we consider the Co(0001) surface using the model of Feibelman and Eastman (Sect. IV.B in [42]) for the calculation of the elastic attenuation lengths $a_{\uparrow\downarrow}$ and an interpolation between Fe and Ni based on the calculations of Hong and Mills [37,41] for the IMFPs of Co [43]. At the vacuum level $a_\uparrow \approx 0.35$ nm, $a_\downarrow \approx 0.30$ nm, at the spin-up band onset at 0.9 eV (see Fig. 6.1) $a_\uparrow \to \infty$ while $a_\downarrow \approx 0.38$ nm vs. $l_\downarrow \approx 0.31$ nm. At the spin-down band onset at 2.0 eV, where also $a_\downarrow \to \infty$, $l_\downarrow \approx 0.33$ nm. This shows that between the band onsets the elastic attenuation length for spin-down electrons

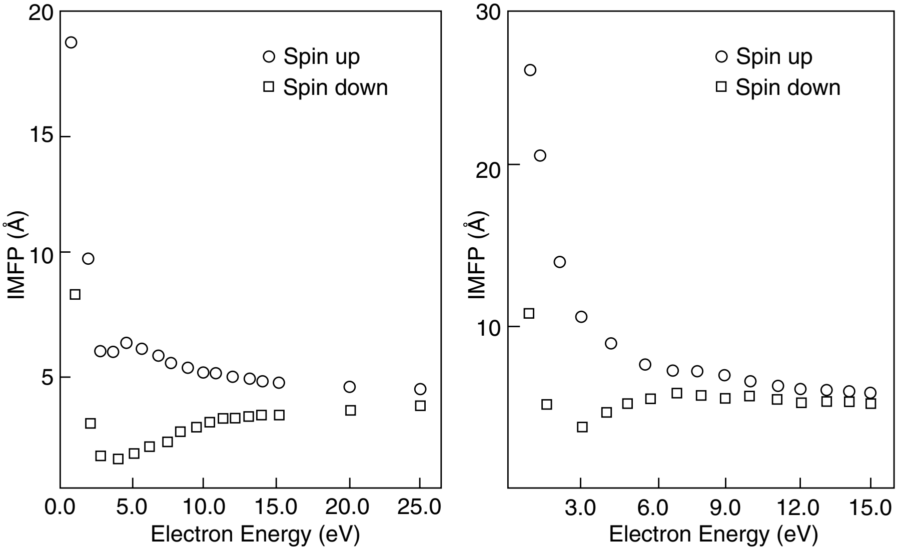

Fig. 6.3. Inelastic mean free paths for spin-up and spin-down electrons in Fe (left) and Ni (right) as a function of electron energy

is sufficiently large, so that significant inelastic damping, that is, reduction of $l_\downarrow$, can occur, resulting in a smaller asymmetry than that in the absence of (inelastic) damping, which is determined by $\boldsymbol{P} \bullet \boldsymbol{M}$. This reduction is, however, apparently insignificant, as several transmission and reflection experiments suggest [44–46]. For example, in Co the contribution of Stoner excitations – which are responsible for the difference of the IMFPs – to the polarization is below 5% for electrons between 5 and 15 eV above the vacuum level [45]. For this reason, inelastic damping is presently taken into account mainly to estimate the sampling depth and the various layer contributions to the signal. The asymmetry is attributed mainly to the exchange potential V_x in the elastic scattering from the ion cores that contain most of the spin density (see for example Fig. 6.1 in [47]). Band gaps caused by the periodic array of the ion cores are relegated into a second place because their influence is largely suppressed by inelastic scattering, as discussed above. In films whose thickness is less than the elastic attenuation length and the IMFP, e.g., in monolayers and double layers, these considerations do not play an important role.

To summarize this section, SPLEEM may be used as a qualitative measure of the magnetization of thin films or of the near-surface region of crystals. Before quantitative conclusions about the magnitude and depth distribution of the magnetization can be drawn from the measured asymmetry, a much better understanding of the elementary interaction processes is necessary. What SPLEEM can do at present is determine the lateral magnetization distribution; in particular, it can image magnetic domains and domain walls.

6.3 Experimental Setup and Procedure

A SPLEEM instrument is a LEEM instrument with a spin-polarized illumination system. The principles and realization of LEEM have been described repeatedly (see, for example [48,49]). Therefore, they will only be sketched briefly. In a LEEM instrument (Fig. 6.4), the object (1) is part of a "cathode" objective lens (2), in which the incident electrons from the illumination system (3) are decelerated from high energies, typically 5–20 keV, to the desired low energy with which they enter the object at (near) normal incidence. After reflection they are reaccelerated in the cathode lens to their original energy – minus possible energy losses in the object. Incident and reflected beams are separated by a magnetic sector field (4) with deflection angles ranging from 20 to 90° in the various instruments. The incident electrons are focused into the back focal plane of the objective lens, so that the illumination of the object is (nearly) parallel. As a consequence, the diffracted electrons produce in this plane the diffraction pattern that is transferred further downstream with a "transfer lens" (5). The angle-limiting aperture (6) is placed into this image of the diffraction pattern. The objective lens images the first image of the object into the center of the beam separator. An intermediate lens (7) allows one to image either the first image of the object or the image of the diffraction pattern in front of the projective lens (8), which produces the final image or diffraction pattern on the microchannel plate – fluorescent screen image detection system (9). The image on the fluorescent screen is recorded with a CCD camera.

In an ordinary LEEM instrument, the illumination system uses a LaB_6 or field emission cathode whose crossover is imaged with 2–3 condenser lenses into the back focal plane of the objective lens. In a SPLEEM system, the electron source is a GaAs(100) surface with high p-doping and negative electron affinity, which is obtained by Cs and oxygen deposition. Spin-polarized electron emission is stimulated

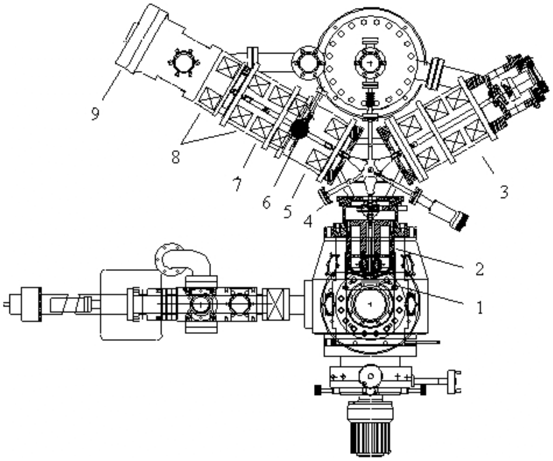

Fig. 6.4. Schematic of a LEEM instrument. For explanation, see text (courtesy C. Koziol)

by illumination with circularly polarized light (σ^+, σ^-), usually from a semiconductor diode laser with a wavelength close to the band gap energy. The conduction band has predominantly s-character and is twofold degenerate ($m_j = -1/2, +1/2$), the valence band has predominantly p-character and is split by spin-orbit interaction into a fourfold degenerate $p_{3/2}$ band ($m_j = -3/2, -1/2, +1/2, +3/2$) and a twofold degenerate $p_{1/2}$ band ($m_j = -1/2, +1/2$). The selection rules and relative transition probabilities give a maximum polarization $P_{\max}$ of 50% of the excited electrons in the crystal. The polarization of the emitted electrons depends on the doping level and profile, on the surface cleaning, in particular, the removal of carbon, and on the activation. 25% to 30% polarization is usual, but P values of close to 50% have also been reported. With strained lattice and quantum well superlattice emitters, P values up to 80% and more have been obtained, though with much lower quantum yield, typically less than 0.1% at the wavelength of maximum P [50]. In contrast, ordinary GaAs emitters may have quantum yields as high as several percent. The vacuum around the emitter is crucial to its lifetime. Less than 1×10^{-10} Torr are needed for lifetimes longer than one day. The science and technology of spin-polarized electron sources has been well reviewed by Pierce [51].

A Pockels cell allows one to switch rapidly between σ^+ and σ^- light and thus between the sign of the polarization of the emitted electrons ($\boldsymbol{P} \rightarrow -\boldsymbol{P}$). For SPLEEM experiments, one wants not only to change between $\boldsymbol{P}$ and – $\boldsymbol{P}$, but also to be able to orient $\boldsymbol{P}$ in any direction, usually into two orthogonal directions in the surface and one perpendicular to it. This can be done with a spin manipulator that is schematically shown in Fig. 6.5 [52]. The combined electrostatic-magnetic 90° deflector, together with the Pockels cell, allow one to orient $\boldsymbol{P}$ in any direction in the plane of deflection by changing the ratio of electrostatic to magnetic deflection. Whenever $\boldsymbol{P}$ has a nonzero transverse component, it can be rotated around the optical axis by changing the magnetic field of the axial-symmetric “rotator” lens. In addition, the spin manipulator contains condenser lenses, deflectors, and a stigmator, as is usual in electron-optical illumination systems. Both presently existing SPLEEM instruments use this principle, but differ in that in one (system A), which is described briefly in [53], the emitter is at high negative potential (-15 kV), while in the other (system B) [54, 55] it is at ground potential, which requires different design in detail.

The next instrument component is the beam separator. In system A, it is a single magnetic deflection field with circular boundary and a semi-circular cutout that acts as a nearly non-focusing 60° deflector. In system B, the beam separator is split into three segments, each deflecting 45° in order to fit the instrument onto a 6-inch flange. Stigmators are needed in both systems to correct for the residual astigmatism. The fields are weak enough, so that the spin precession in them may be neglected. The heart of the instrument is the objective lens that produces the first image and the diffraction pattern, in addition to decelerating and reaccelerating the electrons in front of the object. Both instruments use an electrostatic tetrode lens that has only slightly larger aberrations than magnetic lenses, but significantly smaller ones than the electrostatic triode lens originally used. The aberrations, in particular, the chromatic aberration, determine the resolution limits, which are shown in Fig. 6.6, as a function of the start energy of the electrons for an energy half-width of 0.5 eV. At a typical

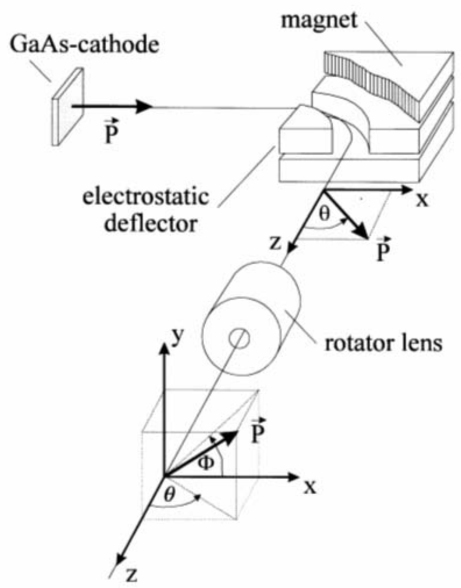

Fig. 6.5. Schematic of the spin manipulator used in the existing SPLEEM instruments

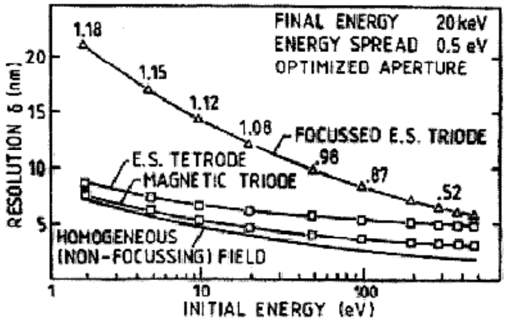

Fig. 6.6. Resolution of various cathode lenses as a function of electron energy. The numbers are typical voltages on the center electrode needed for focusing

SPLEEM energy of 2 eV, a resolution of 8 nm could be expected with the tetrode lens, but in practice it is usually larger than 10 nm.

The magnetic contrast is proportional to $\boldsymbol{P}\bullet\boldsymbol{M}$. Separation of the magnetic contrast from the structural contrast requires the acquisition of two images with opposite polarization ($I_\uparrow$, $I_\downarrow$) and their subtraction from each other. In order to normalize these images, the difference image is divided by the sum image. This results in an image that is proportional to the asymmetry $A : PA = P(I_\uparrow - I_\downarrow)/(I_\uparrow + I_\downarrow)$. When $I_\downarrow > I_\uparrow$, A is negative. Furthermore, the magnetic contrast is usually small compared with the structural contrast. Therefore, the final magnetic image is displayed in the form

$$A^* = N/2 + C(I_\uparrow - I_\downarrow)/(I_\uparrow + I_\downarrow)\,. \tag{6.5}$$

Here, N is the number of gray levels of the CCD camera and C is a contrast enhancement factor chosen in such a manner so that no pixel in the final (A^*) image is saturated. During routine studies, image subtraction is done on-line, which sometimes causes loss of resolution or artificial contrast due to specimen shifts between two images. Typical image acquisition times range from 1 to 5 sec per image. Image shifts can be eliminated by off-line processing with suitable algorithms. A purely structural image is obtained from $I_\uparrow + I_\downarrow$.

In view of the fact that the magnetic contrast is proportional to $\boldsymbol{P} \bullet \boldsymbol{M}$, $\boldsymbol{P}$ is chosen to be parallel and anti-parallel to $\boldsymbol{M}$ for easy analysis if there is a strong in-plane magnetic anisotropy and similarly perpendicular to the surface in the case of pure out-of-plane magnetization. In general, $\boldsymbol{M}$ shows a more complicated angular distribution, so images with three $\boldsymbol{P}$ directions have to be taken for complete analysis. In the case of uniaxial in-plane anisotropy, for example, Néel domain walls can be imaged with $\boldsymbol{P}\perp\boldsymbol{M}$. These procedures are illustrated in Fig. 6.7 for an eight-monolayer-thick epitaxial Co film on W(110), which has a strong uniaxial in-plane anisotropy with the easy axis in the [−110] direction. Whenever the direction of $\boldsymbol{P}$ is changed, the illumination conditions are changed somewhat due to imperfections

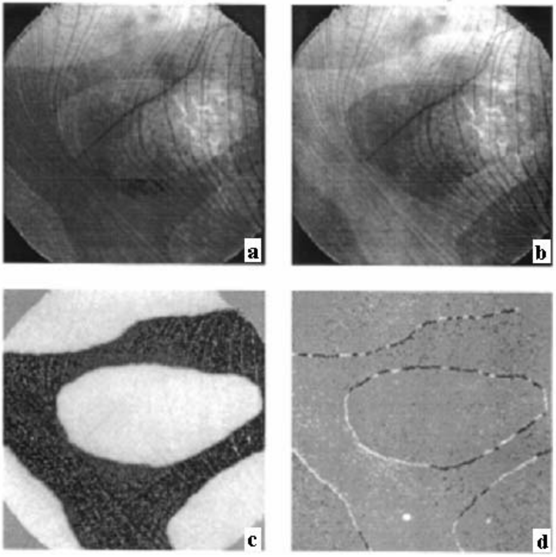

Fig. 6.7. SPLEEM images of a 6 monolayer thick Co layer on W(110). (**a**) and (**b**) are the two images taken with opposite polarization parallel to the easy axis, (**c**) the contrast-enhanced difference image, and (**d**) the difference image, of images taken with in-plane polarization perpendicular to the easy axis. Field of view 13 μm

in the illumination system and in the alignment of the laser beam (Pockels cell switching) and the electron beam. These can be largely corrected with deflectors, but usually cause some intensity changes that are eliminated in the final magnetic image by the normalization procedure described above.

As discussed in Sect. 6.2, SPLEEM gives at least a relative measure of the magnetization averaged with an exponential damping factor over the sampling depth. In thin films that show a spin-dependent quantum size effect, it is in principle possible to obtain information on the perpendicular magnetization distribution by shifting the nodes and antinodes of the waves via changing the energy once the necessary theory is developed.

6.4 Applications

6.4.1 Single Layers

Single layers were studied with SPLEEM mainly in order to understand i) how the magnetic domain structure and the magnetization direction evolve with increasing film thickness, ii) how they are influenced by substrate defects, and iii) how they are modified by segregated and deposited thin nonmagnetic overlayers. Most of the work has been done on Co on W(110), followed by Co on Au(111) and W(111). Fe on Cu(100) has also been a subject of recent studies. In the early Co/W(110) studies, two phases of Co were observed: fcc Co with the (100) plane parallel to the substrate in two equivalent azimuthal orientations and hcp Co with the epitaxial orientation $(0001)_{\mathrm{Co}} \parallel (110)_{\mathrm{W}}$, $[-1100]_{\mathrm{Co}} \parallel [-110]_{\mathrm{W}}$ [56]. The former developed from a poorly ordered film deposited at room temperature on carbide-covered surfaces upon annealing to 530 K and showed magnetic domains with several gray levels, that is, no preferred magnetization direction. The hcp phase was obtained on the clean surface, was also well-ordered when deposited at room temperature and showed a pronounced in-plane anisotropy with the easy axis along the W[-110] direction. In this direction, the misfit is small, so the layer is dilated by 2.4% into a one-dimensional pseudomorphy, while in the W[001] direction, the misfit is large, so the layer is one-dimensionally floating. The strong magnetic anisotropy was attributed to the strain in the W[-110] direction. In both phases, magnetic contrast appeared at 3 monolayers (ML) and increased up to at least 6 ML. In this early work, $\boldsymbol{P}$ could be rotated only parallel to the surface. Once the spin manipulator was also available, the out-of-plane component of $\boldsymbol{M}$ became accessible. This led to the discovery that Co layers on clean W(110) also had an out-of-plane $\boldsymbol{M}$ component (Fig. 6.8) [57]. The deviation of the resulting $\boldsymbol{M}$ direction from in-plane magnetization decreased from about 36° at 3 ML to about 6° at 8 ML in an apparently oscillatory manner and was practically zero at 10 ML. As also seen in Fig. 6.8, the domain boundaries of the in-plane $\boldsymbol{M}$ images are little influenced by the monatomic substrate steps (Fig. 6.8a), while the domain boundaries of the out-of-plane $\boldsymbol{M}$ images in general coincide with substrate steps (Fig. 6.8b). Neither of them is influenced by the thickness variation in the three atomic level system consisting of 4, 5, and 6 ML thick regions, which

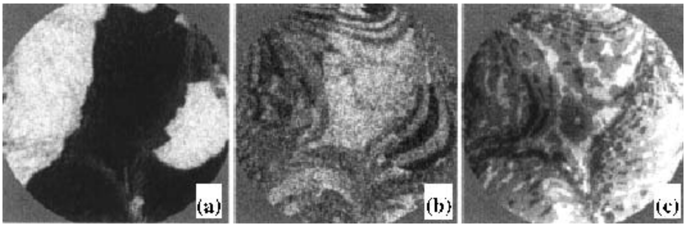

Fig. 6.8. SPLEEM images of the in-plane (**a**) and out-of-plane (**b**) magnetization components, taken with 1.2 eV electrons, and LEEM quantum size contrast image (**c**) taken at 3 eV of a five-monolayer-thick Co layer on W(110). Field of view 6 μm

are made visible by quantum size contrast in the LEEM image of Fig. 6.8c. The out-of-plane ***M*** component alters sign from monatomic terrace, to monatomic terrace so that a wrinkled magnetization results. The thickness dependence of the tilt angle of ***M*** was attributed to the influence of the second and fourth order interface anisotropy between Co and W. The sign change of the out-of-plane ***M*** component is due to the minimization of the dipolar energy, and its preferred occurrence at steps is caused by local anisotropies at steps at which there is a strong misfit perpendicular to the surface.

In addition, the evolution of the direction of ***M*** in island films with increasing thickness or temperature was studied [58]. At elevated temperature, but below the temperature at which alloying starts ($\approx$ 800 K) Co grows on W(110) in the Stranski-Krastanov mode with three-dimensional islands in a closely packed monolayer sea. The islands nucleate preferentially at W mesas, the remnants of previous alloying accidents, and grow preferentially in the floating layer direction W[001] (Fig. 6.9a). Independent of the aspect ratio of the islands ***M*** points in the easy direction (W[-110], Fig. 6.9b), indicating that the magnetoelastic anisotropy is in all cases larger than the shape anisotropy. For this reason, it is not surprising that the local magnetization is preserved when a thin continuous quasi-two-dimensional layer breaks up into many small three-dimensional islands upon annealing [58].

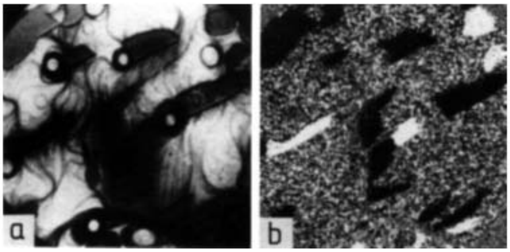

Fig. 6.9. LEEM image (left) and SPLEEM image (right) of a Co layer grown on W(110) at 790 K. The flat but three-dimensional Co crystals nucleate preferentially at W mesas and grow preferentially in the W[001] direction. Field of view 14 μm

One of the most interesting phenomena in quasi-two-dimensional layers are the standing waves in them that cause the quantum size oscillations discussed in Sect. 6.2 (Fig. 6.2). Standing waves in ferromagnetic films have become popular in connection with the interlayer coupling that will be discussed later. SPLEEM offers the possibility to study them with atomic depth.

The W(110) surface is atomically rather smooth and allows the Co layer to approach the bulk structure relatively fast. In contrast, the W(111) surface is atomically rough and imposes its lateral periodicity onto the growing Co film over a number of atomic layers, which depends upon the growth temperature [59]. Because of the large difference between the atomic diameters ($d_{\mathrm{Co}} = 0.251\,\mathrm{nm}$, $d_{\mathrm{W}} = 0.274\,\mathrm{nm}$), this pseudomorphic (ps) layer is strongly contracted perpendicular to the surface, so that three successive ps Co layers may be considered as a strongly corrugated Co(0001) layer with somewhat smaller packing density (17.30×10^{14} atoms/cm^2) than a Co(0001) layer in the bulk (18.37×10^{14} atoms/cm^2). On the basis of this consideration, one would expect no preferred $\boldsymbol{M}$ direction in the layer because the in-plane magnetocrystalline anisotropy of the Co(0001) plane is very small. The first experiments, however, showed a pronounced uniaxial anisotropy with large domains. This has been attributed to a slight miscut indicated by a small elongation of the LEED spots. On a second crystal that showed sharp LEED spots, small domains with several $\boldsymbol{M}$ orientations were observed whose size, shape, and distribution depended strongly upon the deposition conditions. This is compatible with negligible in-plane anisotropy and nucleation of non-interacting magnetic domains in different surface regions at zero external fields. On both substrates, the asymmetry is zero up to about ps 7 ML, then rises rapidly up to 8–9 ps ML and thereafter at a lower rate linearly up to the largest thickness studied (12 ps ML). Extrapolation to zero magnetic signal suggests that the first three ps ML, which correspond to less than one close-packed Co(0001) layer is nonmagnetic [32], at least at room temperature, similar to Co on W(110) [60]. This is not surprising in view of the strong hybridization of the $3d$ bands of the Co monolayer with the $5d$ bands of the W substrate, which causes a shift of the bands to lower energies, so that the minority spin states become more strongly occupied [61].

Co layers on W(100) have been studied only in a cursory manner because of their pronounced three-dimensional growth beyond 2–3 pseudomorphic monolayers. The Co crystals form long crystals with the (11–20) plane parallel to the substrate and the [0001] directions parallel to the W $\langle 011 \rangle$ directions. The first two monolayers were found to be nonmagnetic. From the crystals, weak magnetic contrast could be obtained only in films grown at room temperature. The long narrow crystals apparently have no (11–20) top faces, as judged by LEEM, so no specular beam and, therefore, no magnetic contrast could be obtained from them [59].

The SPLEEM study of Co films on Au(111) was motivated by SEMPA studies (see Chap. 7) of the same system in which the spin reorientation transition (SRT) with increasing coverage had initially been interpreted by a continuous $\boldsymbol{M}$ rotation within the domains [62], and later by a decay of the domain size and the coexistence of in-plane and out-of-plane domains in a narrow thickness range [63]. These studies were made in large thickness steps [62] or with wedges, in which the SRT took place

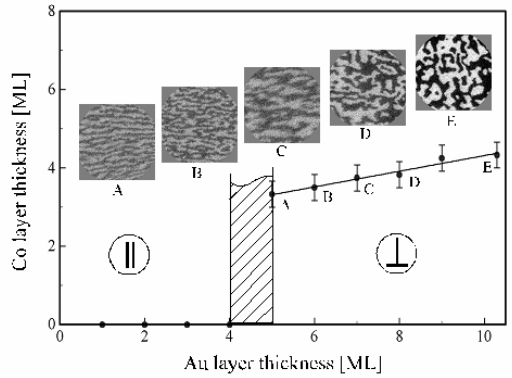

Fig. 6.10. Magnetization direction in thin Co layers on epitaxial Au layers on W(110) as a function of Au and Co thickness. To the left and above line AE the magnetization is predominantly in-plane. The inserts show the domain structure at the Au coverages corresponding to A–E and at Co film thicknesses increasing from 2.8 to 4.3 ML from A to E. Field of view 9–10 μm

within a narrow region [63–65]. The much faster image acquisition with SPLEEM allows a quasi-continuous study of the SRT during growth in much finer thickness steps and gives a more detailed picture of the SRT. In the SPLEEM study, (111)-oriented epitaxial layers on W(110) were used as substrates [66]. Previous work [67] had shown that the domain structure and the SRT depend on the thickness of the Au, layer. In particular, at 2 ML Au, the domain structure was strongly influenced by the substrate steps. Therefore, the dependence of the domain structure on the thickness of the layer was studied in more detail [68]. ***M*** was found to be in-plane up to 4 ML Au. From about 5 ML Au upwards, it is out-of-plane up to a Au thickness-dependent Co thickness. This is indicated in Fig. 6.10, which also shows the out-of-plane domain structure in this region. Initially, when the anisotropic strain in the Au film still influences the domain structure, it is a striped phase, but with increasing Au thickness it develops into a more droplet-like phase, which is taken as an indication that the Au surface is nearly bulk-like at 10 ML Au.

On this surface, the SRT was studied in thickness increments as small as 0.05 ML [66]. The domain size was found to increase up to about 4 ML in agreement with [37] and with theoretical predictions that assume thin walls whose width is independent of thickness and small compared to the domain size [69]. The actual SRT takes place between 4.2 and 4.4 ML (Fig. 6.11). A detailed analysis of the correlation between the domain walls in the out-of-plane ***M*** images and of the domains in the in-plane ***M*** images [66] shows that the transition occurs via widening of the out-of-plane domain walls accompanied by a breakup of the out-of-plane domains. This scenario can be described to a first approximation by the Yafet-Gyorgy model [70]. Recently, Monte Carlo model calculations of the SRT also predicted wall broadening, but with a more complicated, twisted spin structure that develops into a vortex structure with decreasing perpendicular to dipolar anisotropy ratio [71]. Experiment shows neither a twisted structure during the transition nor a vortex structure above the transition.

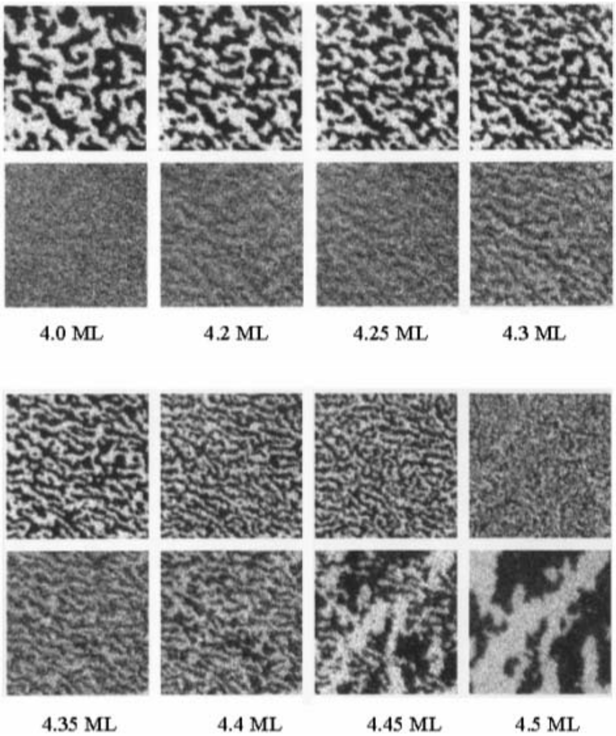

Fig. 6.11. Spin reorientation transition in a Co layer on a 10 ML thick Au(111) layer on W(110). Upper rows: out-of-plane, lower rows: in-plane magnetization images taken with 1.2 eV electrons. Coverage range 4.0–4.5 ML. Field of view 7 × 7 μm

The fact that above the transition the layer has uniaxial anisotropy similar to the layer grown directly on W(110) suggests that the twisted phase is suppressed by a still noticeable strain in the Au layer. Alternatively, the twisted phase could be a small-size or relaxation time effect in the Monte Carlo simulations. This is suggested by the fact that after long relaxation times only one vortex is left in the disk-shaped samples that is the lowest energy configuration for small samples. It is interesting to note that the evolution of the domain structure in the in situ SPLEEM [66] study agrees well with that of the ex situ SEMPA study of the annealed wedge that was covered with Au. Apparently during the slow growth used in the SPLEEM experiment, Au diffused onto the surface of the growing Co layer.

The magnetic properties and structure of Fe layers on Cu (100) have been the subject of many investigations, including a SEMPA study [72], because of their interesting dependence of structure and magnetism upon thickness, deposition conditions, and temperature, but the physical origin of this dependence is still not fully understood. SPLEEM is ideally suited to elucidate the connection between structure and magnetization. The system Fe/Cu(100) is a good example [34]. Fe films were grown in SPLEEM system B (see Sect. 6.2) at room temperature at deposition rates rang-

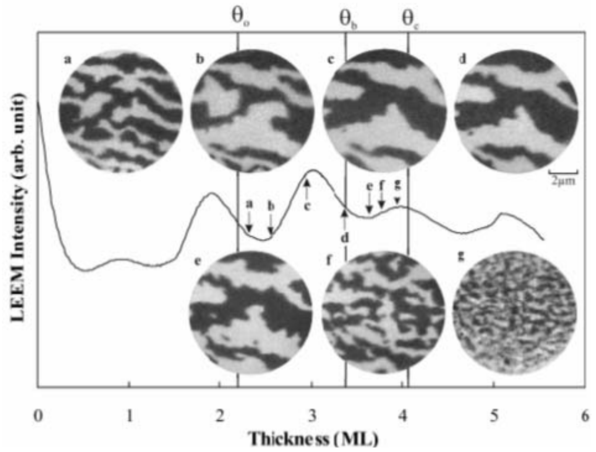

Fig. 6.12. LEEM intensity oscillations and out-of-plane magnetization images of a Fe layer on Cu(100) as a function of thickness taken with 1.8 eV electrons. Field of view 9 μm

ing from 0.07 to 0.49 ML/min. Figure 6.12 shows the LEEM intensity oscillations connected with layer-by-layer growth and out-of-plane SPLEEM images taken at the thicknesses marked by arrows. The lines marked by θ_a, θ_b, and θ_c indicate the onset of magnetism, the breakup of the domains, and the disappearance of magnetism, respectively. The asymmetry deduced from the SPLEEM images rises sharply from zero at 2 ML and becomes zero again at 4 ML. This is attributed to T_c being below room temperature in both cases. According to previous studies, the layer becomes antiferromagnetic above 4 ML with a ferromagnetic monolayer on top that has a low T_c. The Curie temperature and the decay of the magnetic domain structure during the approach of T_c could also be determined from the asymmetry. The dependence of the asymmetry upon thickness could be well fitted by the product of thickness and magnetization, taking into account the thickness dependence of the Curie temperature and assuming the two-dimensional Ising model for the temperature dependence of the magnetization, together with some broadening caused by nonuniform thickness. This supports the stipulation made in Sect. 6.2 that the asymmetry should be a measure of magnetization at least in very thin films.

6.4.2 Nonmagnetic Overlayers

Nonmagnetic overlayers change the surface anisotropy and, therefore, also the direction of $\boldsymbol{M}$. A strong enhancement of the perpendicular anisotropy at 1–2 ML has been reported for a number of overlayers, including Au and Cu [73]. As the magnetic anisotropy arises mainly from spin-orbit coupling, it is not a priori clear why this enhancement should occur, and why it should be different in different studies of the same system. The structure of the overlayer seems to play an important role, and SPLEEM is a good technique to correlate it with the change of $\boldsymbol{M}$. The influence of Au layers on Co layers on W(110) was studied as a function of Co layer thickness at

400 K, that of Cu layers on Co on W(110) as a function of temperature at constant Cu thickness. In both cases, no change in the magnetic domain size was observed, only a rotation of $\boldsymbol{M}$ toward the surface normal. In the case of Au overlayers, the perpendicular anisotropy increased with Au thickness up to 1.5–2 ML without a maximum for Co layers from 3–6 ML, and with a weak maximum at 2 Au ML on thicker films. This could be attributed to double layer island growth at this temperature. Cu overlayers, however, produced a clear maximum of the perpendicular anisotropy at coverages from 1 to nearly 2 ML, depending on growth temperature between room temperature and 430 K. The structure of the layer depended strongly upon temperature. At 365 K, the Cu islands were large enough so that the anisotropy could be measured locally. Initially, monolayer islands formed, on which at about 1.2 ML double layer islands grew. The enhanced perpendicular anisotropy appeared only in the monolayer regions and decreased in the 3 ML thick regions to the original value of the clean surface. Inasmuch as the layer structure depends strongly upon the growth conditions, the maximal enhancements vary with them. This explains the differences between different studies.

6.4.3 Sandwiches

It is well established that the interlayer coupling between two ferromagnetic layers through a non-ferromagnetic spacer layer depends strongly on the microstructure of the layers, in particular, of their interfaces. The coupling is usually collinear and oscillates with increasing spacer thickness between ferromagnetic (FM) and antiferromagnetic (AFM), but frequently non-collinear or 90° coupling is observed, too. This non-collinear coupling is due to a biquadratic coupling contribution to the interlayer exchange energy

$$E = J_1(1 - \cos\phi) + J_2(1 - \cos^2\phi)\,, \tag{6.6}$$

in addition to the usual bilinear coupling that is responsible for the collinear coupling. Roughness causes spacer thickness fluctuations and magnetic dipoles. If some intermixing between ferromagnetic and spacer layers occurs, loose spins are created at the interface or in the spacer. All these phenomena can produce "extrinsic" biquadratic coupling [74–77], in addition to the "intrinsic" biquadratic coupling through atomically flat spacers. The intrinsic coupling is, however, too weak to explain the experimental observations. A deeper understanding of the influence of the roughness on the non-collinear coupling is, therefore, desirable. SPLEEM is well-suited for the correlation between roughness and magnetic structure.

Two systems have been studied: Co/Au/Co epitaxial sandwiches [78] and Co/Cu/Co epitaxial sandwiches [79], both on W(110). In all cases, the bottom Co layer was 7 ML thick, so it still had a small perpendicular $\boldsymbol{M}$ component (see Fig. 6.8). This allowed the simultaneous measurement of the coupling of perpendicular and in-plane magnetization. On top of the Co layer, Au layers were deposited in monolayer steps ranging from 3 to 8 ML, with some intermediate thicknesses of special interest. All layers except a few were deposited at room temperature to minimize roughness caused by three-dimensional crystal formation and intermixing. A few were deposited at about 400 K to check the influence of this roughness. The evolution of the domain structure in the top layer was followed in steps of one monolayer. The results will be illustrated now for Au spacers.

In the thickness range studied, the system Co/Au/Co with Au(111) orientation is known to have AFM coupling at about 5 ML and FM coupling below and above this thickness. This is confirmed by the SPLEEM studies that show, however, a more complicated coupling, as illustrated in Figs. 6.13 and 6.14 for FM and AFM coupling, respectively. In Fig. 6.13, the spacer layer is slightly more than 6 ML thick. The top row shows the domain structure images of the bottom layer with $\boldsymbol{P}$ parallel to the easy axis, hard axis, and perpendicular to the surface, respectively. In the out-of-plane $\boldsymbol{M}$ image, the contrast of the small domains of the perpendicular $\boldsymbol{M}$ component is small and no domains are recognizable in regions of high step density that were located before the deposition. Six Au ML attenuate the magnetic signal only slightly because of the large spin-independent inelastic mean free path in Au. However, already 1 Co ML causes a strong attenuation. At 2 and 3 Co ML, no in-plane signal is seen at all, while a strong perpendicular image contrast develops already at 2 ML, as expected for Co on Au (see Sect. 6.4.1). The second row in Fig. 6.13 shows the three images at 3 Co ML. At 4 ML Co, weak easy-axis contrast is already present, although the out-of-plane contrast is still strong, differing from the spin reorientation transition on Au without a Co underlayer. This is attributed to interlayer coupling. The influence of the substrate steps on the out-of-plane image that is still slightly seen at 2 Co ML has

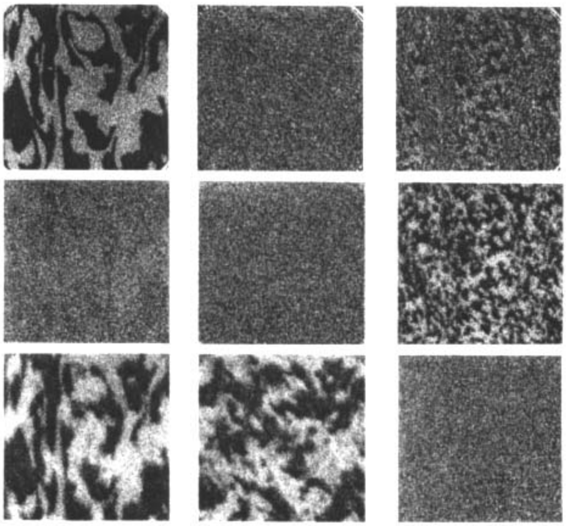

Fig. 6.13. In-plane easy axis (left), hard axis (center), and out-of-plane (right) SPLEEM images of a Co/Au/Co sandwich with ferromagnetic interlayer coupling taken with 1.2 eV electrons. The thickness of the top Co layer is from top to bottom 0, 3, and 7 ML. Room temperature deposition. Field of view 6 × 6 μm

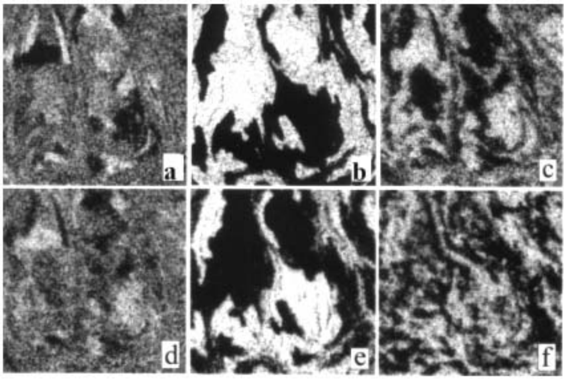

Fig. 6.14. SPLEEM images of a Co/Au/Co sandwich with antiferromagnetic coupling. Room temperature deposition. Energy and field of view as in Fig. 6.13. For explanation, see text

disappeared at 3 Co ML, so that not only FM-coupled domains are found above the domains in the bottom layer, but also domains, though smaller, in regions with high substrate step density. From 4 to 5 ML, the domain structure changes dramatically, as shown in the third row. The out-of-plane image has disappeared due to the SRT and has been replaced by a domain pattern in the hard-axis direction, while simultaneously the easy-axis image contrast has increased. This domain structure persists up to the highest Co thickness studied (8 ML), except for a slight coarsening of the hard-axis domain structure. If the gray levels are taken as a measure of the magnitude of the $\boldsymbol{M}$ components and the in-plane components are added vectorially, a complicated domain structure with the $\boldsymbol{M}$ directions inclined $+/-45°$ toward the easy axis in the bottom film arises, that is, the top layer shows non-collinear coupling with the bottom layer. Under the experimental conditions of this experiment, the layers are believed to grow as a three-level system, though with much smaller terraces than those shown in Fig. 6.8c, with the top face of the Au layer reproducing reasonably well the fluctuations of the top face of the bottom Co layer and with little intermixing, so that the non-collinear coupling most likely is of the dipolar type.

In the case of AFM coupling, the domain structure develops with thickness in the same manner as in the case of FM coupling. Figure 6.14 shows a few stages of this evolution for a spacer thickness of about 5 ML. Images (a) and (b) are out-of-plane and easy-axis in-plane images, respectively, of the bottom layer. The substrate region selected had a high density of atomic steps, so only a few domains can be recognized in the out-of-plane image. The out-of-plane image (c) is from a film with 3 Co ML on top of the Au layer. It shows AFM coupling in the regions in which the bottom layer has a perpendicular $\boldsymbol{M}$ component, but also perpendicular magnetization in other regions. Actually, $\boldsymbol{M}$ is not completely perpendicular because there is already a weak AFM-coupled in-plane component, as described above. At 4 Co ML, the out-of-plane $\boldsymbol{M}$ component has already significantly decreased (d) and the easy axis in-plane $\boldsymbol{M}$ component is nearly as large as shown in image (e) from a 6 ML thick top layer with perfect AFM coupling to the bottom layer. Simultaneously with the disappearance of the out-of-plane contrast, an in-plane hard-axis contrast develops, which is shown for the 6 ML thick top layer in image (f). Thus, the scenario for AFM coupling is exactly the same as for FM coupling. When the two in-plane gray levels are vectorially added pixel by pixel for the various spacer thicknesses, the resulting $\boldsymbol{M}$ rotation relative to the $\boldsymbol{M}$ direction in the bottom layer increases from $\phi = 15°$ at 4 Au ML to $\phi = 45°$ at 6 Au ML. With thicker spacers, the rotation angle increases even more, which indicates a biquadratic and bilinear coupling of equal magnitude. The interlayer coupling is quite sensitive to interfacial roughness. For example, in sandwiches grown at about 400 K, which have larger interface roughness, the domain pattern of the top layer shows no sign of in-plane interlayer coupling.

6.4.4 Other Topics

All the results discussed up to now have been obtained from samples prepared in situ. The question arises to what extent samples prepared ex situ can be studied with SPLEEM. In view of the small sampling depth of SPLEEM, contamination and other surface layers reduce or even eliminate magnetic contrast and have to be removed by sputtering or other feasible methods. That this can be done is illustrated by one of the first SPLEEM images taken (Fig. 6.15 [2]). It is from the (0001) surface of a bulk Co crystal that had been cleaned by simultaneous 1.5 keV Ar ion bombardment and annealing at 400 °C. Recent experiments demonstrate that this procedure is also applicable to thin films [80].

Important parameters in magnetic studies are external magnetic fields, temperature, and time. External fields parallel to the sample surface cannot be applied during imaging because they deflect the electron beam. Of course, with fields applied before

Fig. 6.15. SPLEEM image of the magnetic domain structure of a Co(0001) surface taken with 2 eV electrons. Field of view 12 μm

imaging, the remanent state of the sample is accessible. In fields perpendicular to the sample surface that are well aligned with the optical axis, imaging is possible. Only the focal length has to be changed and usually beam and/or sample tilt have to be corrected because perfect alignment is difficult. Without specially designed sample holders, fields are limited to a few hundred Gauss.

Cooling has been achieved up to 118 K in a SPLEEM instrument [80] with liquid nitrogen, but temperatures in the 10 K range should become accessible with liquid helium cooling. Temperatures in the 1 K range appear unrealistic because of the specimen holder/lens configuration, which does not allow effective thermal shielding. Time is an important parameter in connection with switching processes. The present image acquisition times in the 1 sec range can possibly be reduced to the 0.1 sec range with further instrument improvement, so that processes in this time domain range may become accessible to SPLEEM. The short switching times of technological interest are, however, outside the reach of SPLEEM.

6.5 Summary

SPLEEM is a non-scanning magnetic imaging technique that makes use of the spin dependence of the elastic scattering of slow electrons. As the spin dependence increases with decreasing energy, because of the energy dependence of the exchange potential, electrons in the 1 eV range are most useful. In this energy range, inelastic scattering and elastic attenuation in band gaps limit the sampling depth in ferromagnetic metals and alloys to a few monolayers. In nonmagnetic materials without band gaps, the sampling depth is usually considerably larger, as indicated by the "universal curve" of the inelastic mean free path.

The lateral resolution of SPLEEM is limited by the spherical and chromatic aberrations of the objective lens and is in practice presently not better than 10 nm. The vertical resolution is limited by the wavelength of the electrons and allows the imaging of monatomic steps and thickness variations via interference contrast. The dependence of the contrast on interference and diffraction is unique to SPLEEM and makes it an ideal method for the correlation between the magnetic structure, crystal structure, and morphology of the specimen. This strength is at the same time a weakness in the study of amorphous or polycrystalline specimens consisting of small crystals without preferred orientation. On these specimens, the intensity of the back-reflected electrons is distributed over a wide angular range, instead of being focused into a strong specular beam. Image acquisition times increase then from the 1 sec range, characteristic for SPLEEM of single crystalline or highly oriented surfaces, to the range needed in SEMPA.

The connection between the asymmetry obtained from two images with opposite polarization of the incident beam and the magnetization is not straightforward. SPLEEM averages over several monolayers and is at best a measure of the exponentially averaged mean value of the magnetization. In the 1 eV range, the situation is, however, much more favorable for a quantitative connection between asymmetry and magnetization than in the 10 eV range used in SPLEED, in particular, in the monolayer range. At present, a quantitative evaluation of SPLEEM images is possible for the ratio of the various components of the magnetization of a fixed layer thickness and a semi-quantitative comparison of these ratios as a function of layer thickness, temperature, or external field. This gives important data for the dependence of the magnetic domain structure on these parameters, from which the ratio of the various magnetic anisotropies may be deduced.

The incorporation of cooling and external fields in the existing systems and the development of commercial instruments, in which the weak points of the existing experimental systems are eliminated, should open up a wide field for SPLEEM in the future.

Acknowledgement. The development of SPLEEM was supported by the IBM Almaden Research Center and the Deutsche Forschungsgemeinschaft. Its application to thin film studies in the author's group is supported by NSF under grant number DMR-9818296.

References

1. R.J. Celotta, D.T. Pierce, G.-C. Wang, S.D. Bader, and G.P. Felcher, Phys. Rev. Lett. **43**, 728 (1979).
2. M.S. Altman, H. Pinkvos, J. Hurst, H. Poppa, G. Marx, and E. Bauer, Mat. Res. Soc. Symp. Proc. **232**, 125 (1991).
3. J.C. Slater, Phys. Rev. **81**, 385 (1951).
4. P. Hammerling, W.W. Shine, and B. Kivel, J Appl. Phys. **28**, 760 (1957).
5. B. Kivel, Phys. Rev. **116**, 926 (1959).
6. E. Bauer and H.N. Browne, in: Atomic Collision Processes, edit. by M. R. C. McDowell (North-Holland, Amsterdam, 1964), p. 16.
7. H.N. Browne and E. Bauer, unpublished work.
8. P.A.M. Dirac, Proc. Cambridge Phil. Soc. **26**, 376 (1930).
9. J.C. Slater, T.M. Wilson, and J.H. Wood, Phys. Rev. **179**, 28 (1969).
10. J. Kessler: Polarized Electrons (Springer, Berlin, 1985).
11. R. Feder, J. Phys. C: Solid State Phys. **14**, 2049 (1981).
12. R. Feder, Phys. Scripta T4, 47 (1983).
13. R. Feder and H. Pleyer, Surf. Sci. **117**, 285 (1982).
14. C.L. Fu and A.J. Freeman, J. Magn. Magn. Mater. **69**, L1 (1987).
15. G. Waller and U. Gradmann, Phys. Rev B **26**, 6330 (1982).
16. E. Tamura, R. Feder, G. Waller, and U. Gradmann, Phys. Stat. Sol. (b) **157**, 627 (1990).
17. E. Tamura and R. Feder, Solid State Comm. **44**, 1101 (1982).
18. A. Ormeci, B.M. Hall, and D.L. Mills, Phys. Rev. B **42**, 4524 (1990).
19. A. Ormeci, B.M. Hall, and D.L. Mills, Phys. Rev. B **44**, 12369 (1991).
20. K. Wagner, N. Weber, H.J. Elmers, and U. Gradmann, J. Magn. Magn. Mater. **167**, 21 (1997).
21. M. Plihal, D.L. Mills, H.J. Elmers, and U. Gradmann, Phys. Rev. B **51**, 8193 (1995).
22. R. Feder, S.F. Alvarado, E. Tamura, and E. Kisker, Surf. Sci **127**, 83 (1983).
23. G.A. Mulhollan, A.R. Koeymen, D.M. Lind, F.B. Dunning, E. Tamura, and R. Feder, Surf. Sci. **204**, 503 (1988).

24. J. Kirschner, Phys. Rev. B **30**, 415 (1984).
25. H.J. Elmers and J. Hauschild, Surf. Sci. **320**, 134 (1994).
26. T.L. Jones and D. Venus, Surf. Sci. **302**, 126 (1994).
27. H.J. Elmers, Internat. J. Modern Phys. B **9**, 3115 (1995).
28. H.J. Elmers, J. Hauschild, and U. Gradmann, J. Magn. Magn. Mater. 140–144, 671 (1995).
29. H.J. Elmers, J. Hauschild, and U. Gradmann, Phys. Rev. B **54**, 15224 (1996).
30. H.J. Elmers, J. Hauschild, G.H. Liu, and U. Gradmann, J. Appl. Phys. **79**, 4984 (1996).
31. K.L. Man, M.S. Altman, and H. Poppa, Surf. Sci. **480**, 163 (2001).
32. Th. Duden, R. Zdyb, M.S. Altman, and E. Bauer, Surf. Sci. **480**, 145 (2001).
33. E. Bauer, T. Duden, H. Pinkvos, H. Poppa, and K. Wurm, J. Magn. Magn. Mater. **156**, 1 (1996).
34. T. Scheunemann, R. Feder, J. Henk, E. Bauer, T. Duden, H. Pinkvos, H. Poppa, H. and K. Wurm, Solid State Commun. **104**, 787 (1997).
35. M.P. Gokhale, A. Ormeci, and D.L. Mills, Phys. Rev. B **46**, 8978 (1992).
36. M. Plihal and D.L. Mills, Phys. Rev. B **58**, 14407 (1998) and references therein.
37. J. Hong and D.L. Mills, Phys. Rev. B **62**, 5589 (2000).
38. D.L. Abraham and H. Hopster, Phys. Rev. Lett. **62**, 1157 (1989).
39. H.C. Siegmann, Surf. Sci. 307–309, 1076 (1994).
40. J.C. Groebli, D. Oberli, and F. Meier, Phys. Rev. B **52**, R 13095 (1995).
41. J. Hong and D.L. Mills, Phys. Rev. B **59**, 13840 (1999).
42. P.J. Feibelman and D.E. Eastman, Phys. Rev. B **10**, 4932 (1974).
43. E. Bauer, unpublished.
44. M.P. Gokhale and D.L. Mills, Phys. Rev. Lett. **66**, 2251 (1991).
45. D. Oberli, R. Burgermeister, S. Riesen, W. Weber, and H.C. Siegmann, Phys. Rev. Lett. **81**, 4228 (1998).
46. D.L. Abraham and H. Hopster, Phys. Rev. Lett. **59**, 2333 (1987).
47. C. Li, A.J. Freeman, and C.L. Fu, J. Magn. Magn. Mater. **94**, 134 (1991).
48. E. Bauer, Surf. Rev. Lett. **5**, 1275 (1998).
49. E. Bauer, Rep. Prog. Phys. **57**, 895 (1994).
50. T. Nakanishi, S. Okumi, K. Togawa, C. Takahashi, C. Suzuki, F. Furuta, T. Ida, K. Wada, T. Omori, Y. Kurihara, M. Tawada, M. Yoshioka, H. Horinaka, K. Wada, T. Matsuyama, T. Baba, and M. Mizuta, In CP421, *Polarized Gas Targets and Polarized Beams*, edit. by R.J. Holt and M.A. Miller (American Institute of Physics, 1998), p. 300.
51. D.T. Pierce, In: *Experimental Methods in the Physical Sciences*, Vol. 29A, edit. by F.B. Dunning and R.G. Hulet (Academic Press), p. 1.
52. T. Duden and E. Bauer, Rev. Sci. Instrum. **66**, 2861 (1995).
53. E. Bauer, In: *Handbook of Microscopy, Methods II*, edit. by S. Amelinckx, D. van Dyck, J. van Landuyt, and G. van Tendeloo (VCH, Weinheim, 1997) p. 751.
54. K. Grzelakowski, T. Duden, E. Bauer, H. Poppa, and S. Chiang, IEEE Trans. Magnetics **30**, 4500 (1994).
55. K. Grzelakowski and E. Bauer, Rev. Sci. Instrum. **67**, 742 (1996).
56. H. Pinkvos, H. Poppa, E. Bauer, and J. Hurst, Ultramicroscopy **47**, 339 (1992).
57. T. Duden and E. Bauer, Phys. Rev. Lett. **77**, 2308 (1996).
58. H. Pinkvos, H. Poppa, E. Bauer, and G.-M. Kim, In: *Magnetism and Structure in Systems of Reduced Dimension*, edit. by R. F. C. Farrow, B. Dieny, M. Donath, A. Fert, and B.D. Hermsmeier (Plenum Press, New York, 1993), p. 25.
59. K.L. Man, R. Zdyb, Y.J. Feng, C.T. Chan, M.S. Altman, and E. Bauer, to be published.
60. H. Fritsche, J. Kohlhepp, and U. Gradmann, Phys. Rev. B **51**, 15933 (1995).
61. H. Knoppe and E. Bauer, Phys. Rev. B **48**, 1794 (1993).

62. R. Allenspach, M. Stampanoni, and A. Bischof, Phys. Rev. Lett. **65**, 3344 (1990).
63. M. Speckmann, H.P. Oepen, and H. Ibach, Phys. Rev. Lett. **75**, 2035 (1995).
64. H.P. Oepen, Y.T. Millev, and J. Kirschner, J. Appl.Phys. **81**, 5044 (1997).
65. H.P. Oepen, M. Speckmann, Y. Millev, and J. Kirschner, Phys. Rev. B **55**, 2752 (1997).
66. T. Duden and E. Bauer, MRS Symp. Proc. **475**, 283 (1997).
67. M.S. Altman, H. Pinkvos, and E. Bauer, J. Magn. Soc. Jpn **19**, 129 (1995).
68. T. Duden, Ph.D. thesis, TU Clausthal (1996).
69. B. Kaplan and A. Gehring, J. Magn. Magn. Mater. **128**, 111 (1993).
70. Y. Yafet and E.M. Gyorgy, Phys. Rev. B **38**, 9145 (1988).
71. E.Y. Vedmedenko, H.P. Oepen, A. Ghazali, J.-C.S. Lévy, and J. Kirschner, Phys. Rev. Lett. **84**, 5884 (2000).
72. R. Allenspach and A. Bischof, Phys. Rev. Lett. **69**, 3385 (1992).
73. T. Duden and E. Bauer, Phys. Rev. B **59**, 468 (1999).
74. J.C. Slonczewski, Phys. Rev. Lett. **67**, 3172 (1991).
75. J.C. Slonczewski, J. Appl. Phys. **73**, 5957 (1993).
76. S. Demokritov, E. Tsymbal, P. Gruenberg, W. Zinn, and I.K. Schuller, Phys. Rev. B **49**, 720 (1994).
77. R. Arias and D.L. Mills, Phys. Rev. B **59**, 11871 (1999).
78. T. Duden and E. Bauer, Phys. Rev. B **59**, 474 (1999).
79. T. Duden and E. Bauer, J. Magn. Magn. Mater. **191**, 301 (1999).
80. E.D. Tober, G. Witte, and H. Poppa, J. Vac. Sci. Technol. A **18**, 1845 (2000).